

Supporting Information

Self-assembly of Metal/Semiconductor Heterostructures via Ligand Engineering: Unravelling Synergistic Dual Roles of Metal Nanocrystals toward Plasmonic Photoredox Catalysis

Ke-Yi Jiang, Ya-Li Weng, Si-Yi Guo, Yan Yu*, Fang-Xing Xiao*

College of Materials Science and Engineering, Fuzhou University, New Campus, Minhou, Fujian
Province 350108, China.

E-mail address: yuyan@fzu.edu.cn;
fx Xiao@fzu.edu.cn

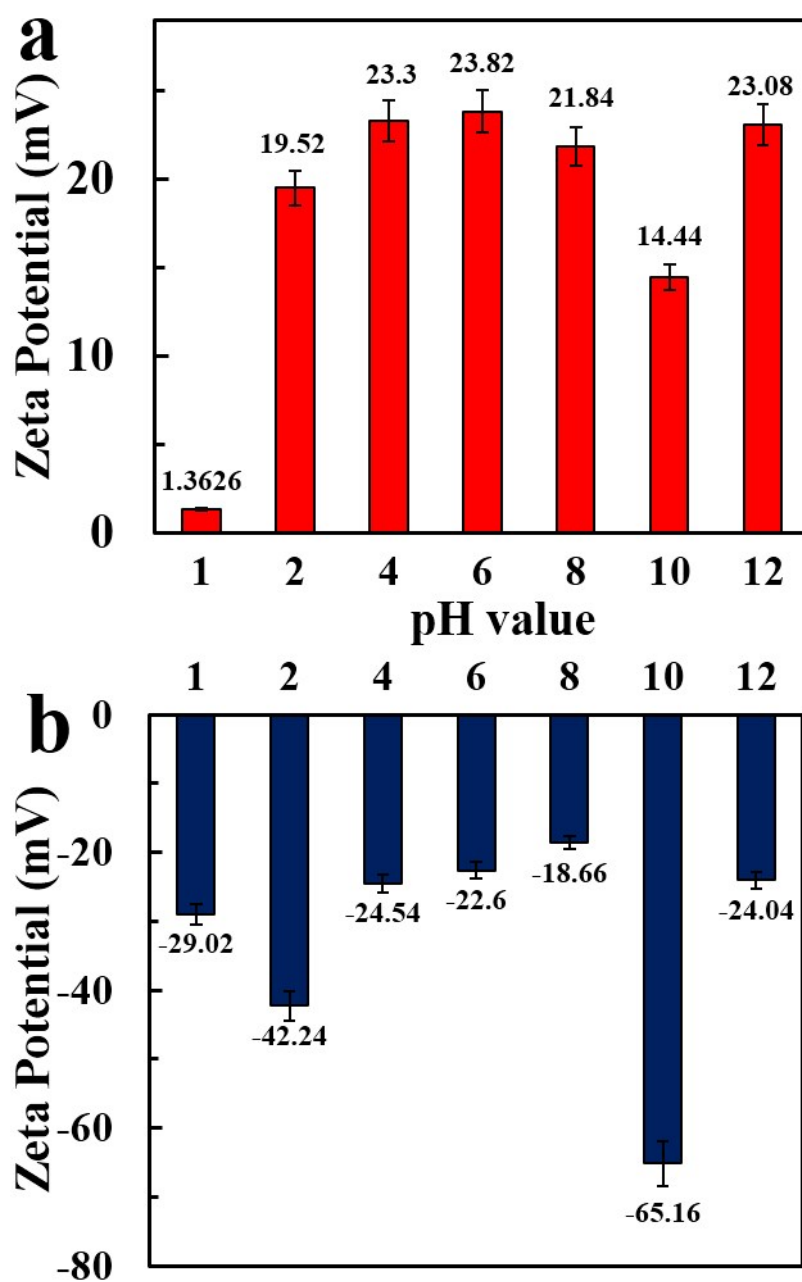


Figure S1. Zeta potentials (ζ) of Au@DMAP (a) and WO₃ NRs (b) aqueous solutions as a function of pH value.

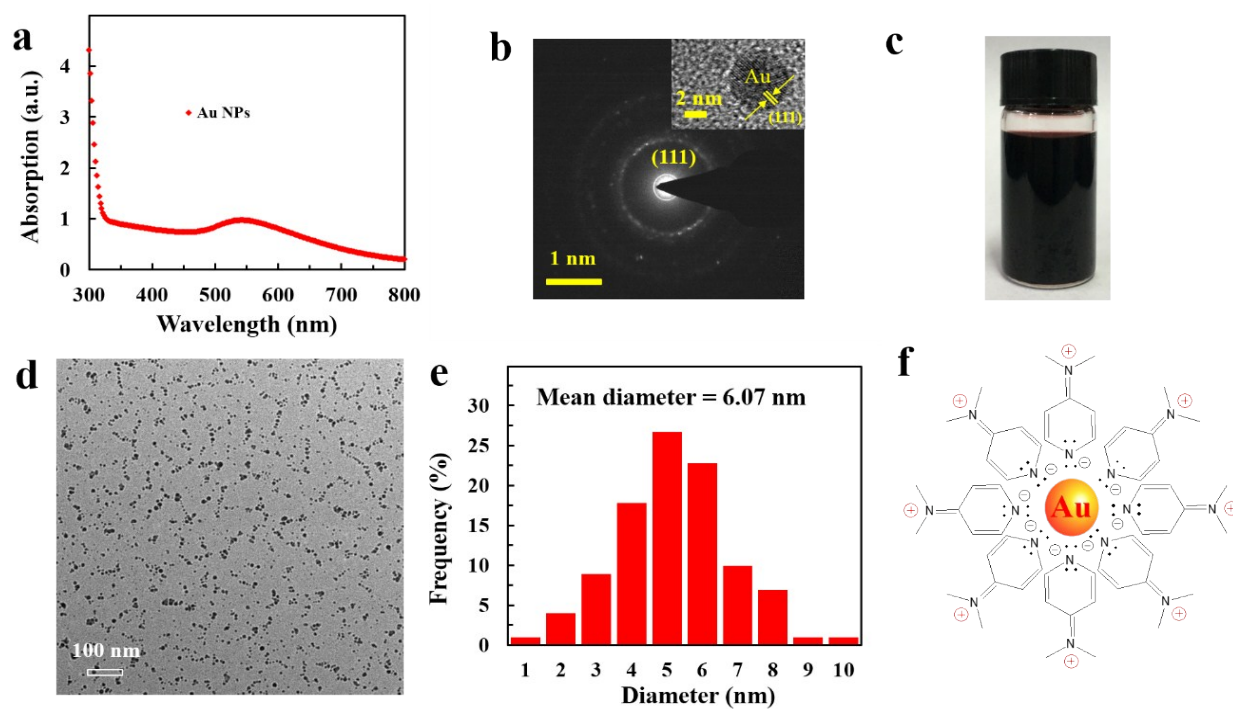


Figure S2. (a) UV-vis absorption spectroscopy and (b) selected area electron diffraction (SAED) pattern of Au@DMAP with corresponding HRTEM image in the inset. (c) Digital photograph, (d) low-magnified TEM image, (e) size distribution histogram and (f) specific molecule structure of Au@DMAP.

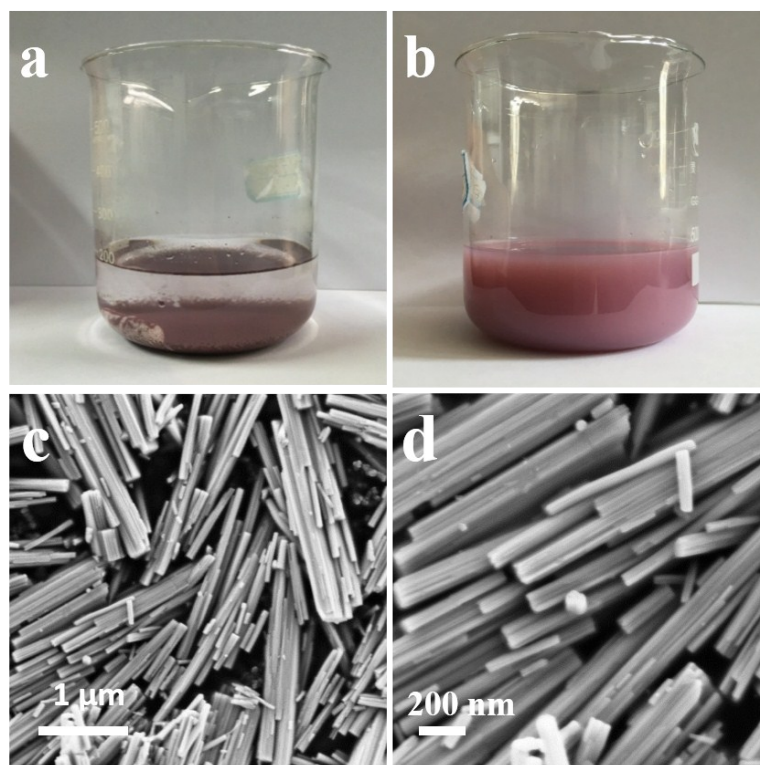


Figure S3. Photographs of (a) Au@DMAP/WO₃ NRs and (b) Au@citrate/WO₃ NRs hybrid suspensions by adding positively charged Au@DMAP and negatively charged Au@citrate dropwise into WO₃ NRs aqueous dispersion with vigorous stirring for 2 h. (c) Low and (d) high-magnified FESEM images of Au-WO₃ NRs nanocomposite obtained by adding Au@citrate into aqueous WO₃ NRs solution in combination with the same low-temperature calcination treatment.

Note: The aqueous solutions of ligand-stabilized Au including Au@DMAP and Au@citrate were added dropwise into the WO₃ NRs aqueous solution under vigorous stirring for triggering the spontaneous self-assembly. The positively charged Au@DMAP can be spontaneously deposited on the WO₃ NRs due to strong electrostatic attraction; contrarily, negatively charged Au@citrate cannot be deposited on the WO₃ NRs by virtue of the substantial electrostatic repulsion. Consistently, as reflected by the experiment phenomena in **Figure S3(a & b)**, no sediment was observed when Au@citrate was added into the aqueous WO₃ NRs solution, which is remarkably different to the phenomenon observed by adding Au@DMAP into aqueous WO₃ NRs solution. The control experiments strongly indicated that inherent surface charge properties of Au NCs play a crucial role in electrostatic self-assembly of plasmonic Au/WO₃ NRs heterostructures.

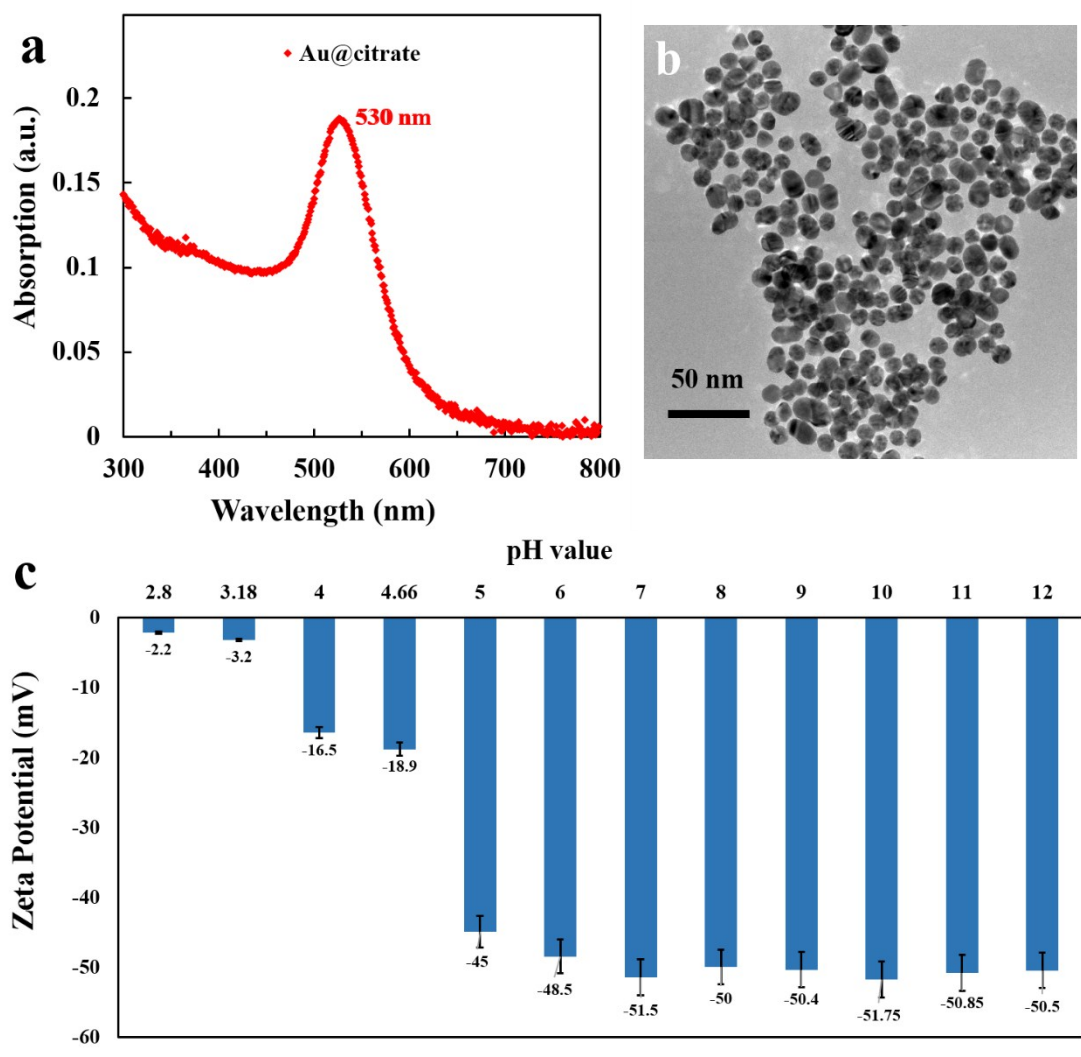


Figure S4. (a) UV-vis absorption spectroscopy, (b) TEM images of Au@citrate NPs, and (c) Zeta potential (ξ) of Au@citrate aqueous solution as a function of pH value

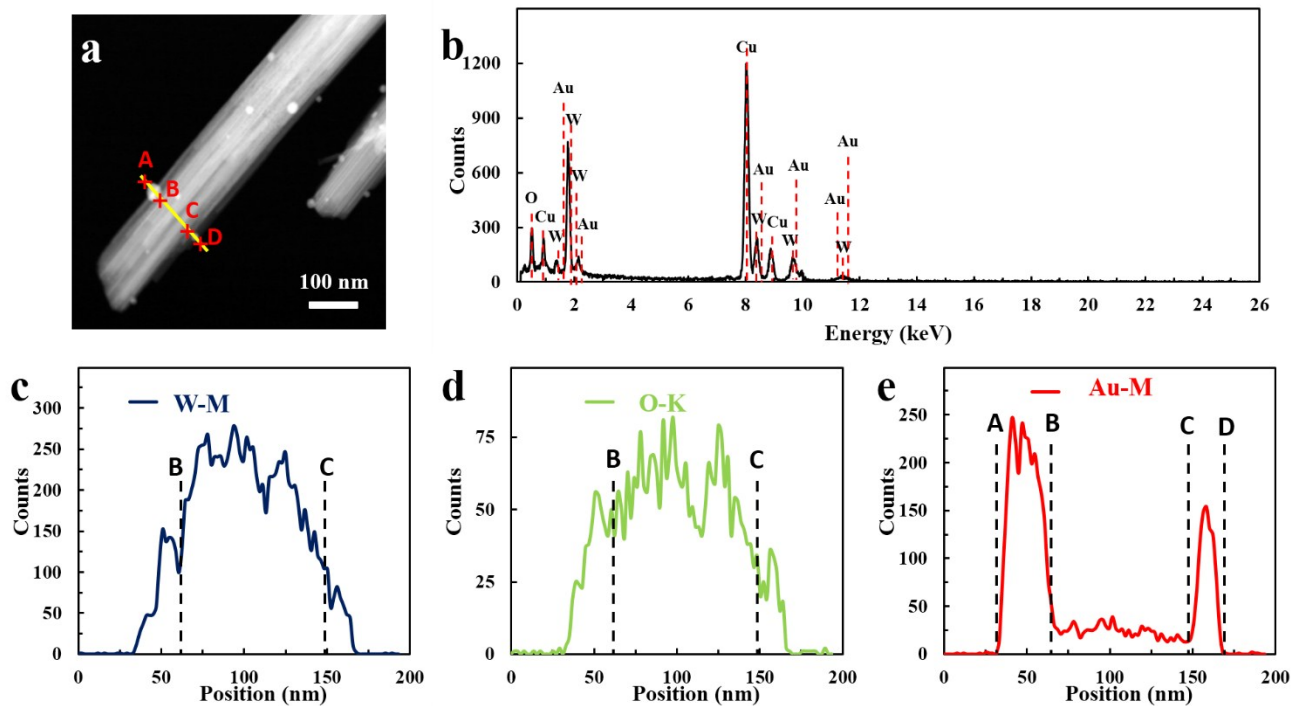


Figure S5. (a) STEM image and (b) EDX analysis of Au-WO₃ NRs heterostructure with corresponding (c-e) linear scanning EDX results.

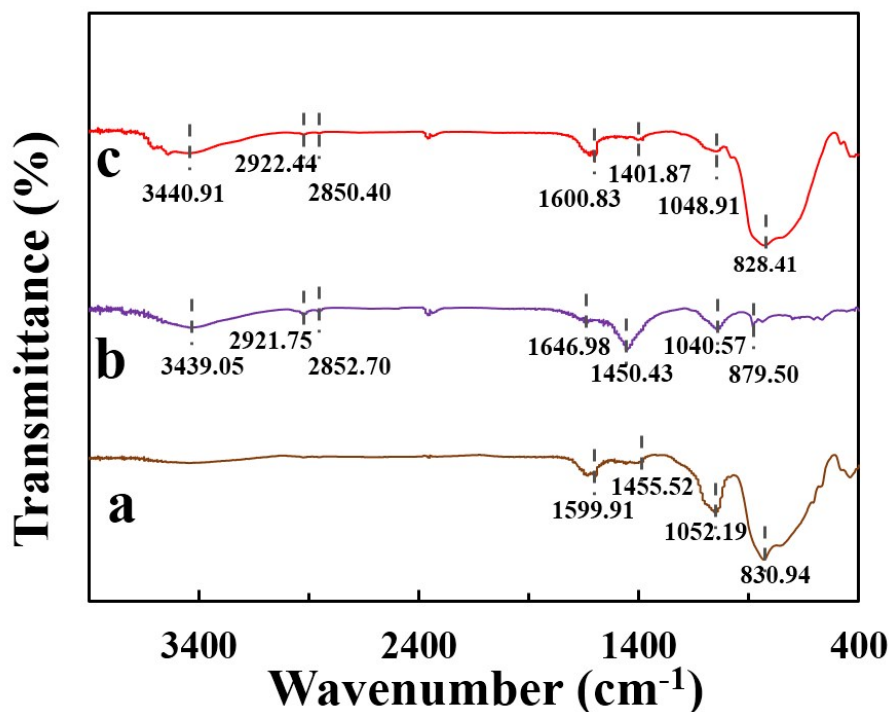


Figure S6. FTIR spectra of (a) WO₃ NRs, (b) Au@DMAP and (c) Au-WO₃ NRs heterostructure.

Note: A typical peak at 828.41 cm⁻¹ was apparently seen in the FTIR spectrum of Au-WO₃ NR nanocomposites (**Figure S6c**) and it corresponds to the stretching vibration mode of W-O-W from WO₃. Compared with FTIR spectrum of WO₃, besides the WO₃ peaks (**Figure S6a**), another two new peaks at 2922.44 and 2850.40 cm⁻¹ were clearly observed in the FTIR spectrum of Au-WO₃ NRs heterostructure (**Figure S6b**), which arise from the stretching vibration mode of -CH₂ group from the remaining surface ligand (DMAP) of Au NPs after calcination. The result strongly confirms the spontaneous self-assembly of Au-WO₃ NRs heterostructure via ligand engineering.

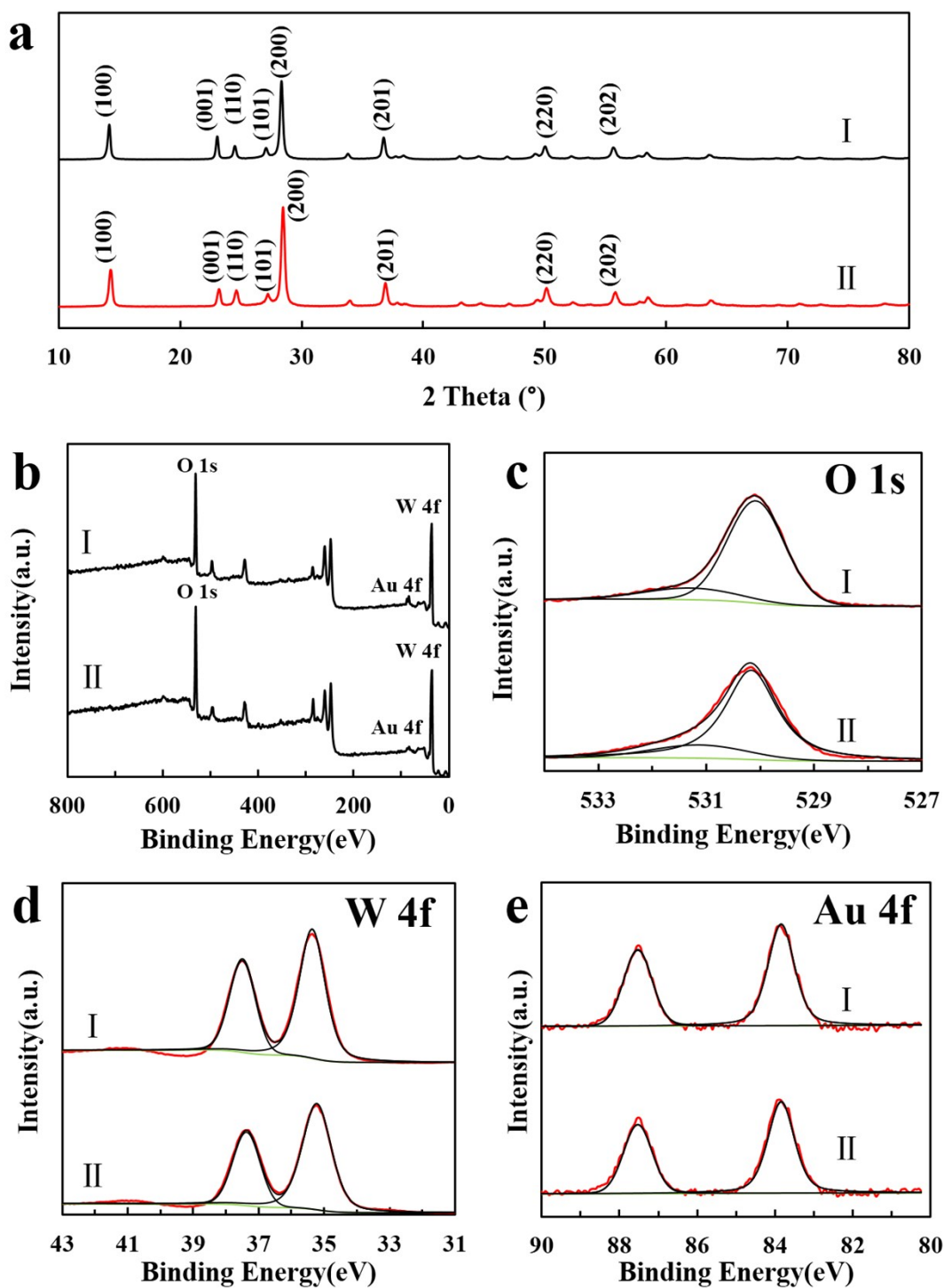


Figure S7. (a) XRD pattern, (b) survey and high-resolution XPS spectra of (c) O 1s, (d) W 4f, (e) Au 4f for 9 wt% Au-WO₃ NRs heterostructure (I) before and (II) after five cyclic photocatalytic reactions.

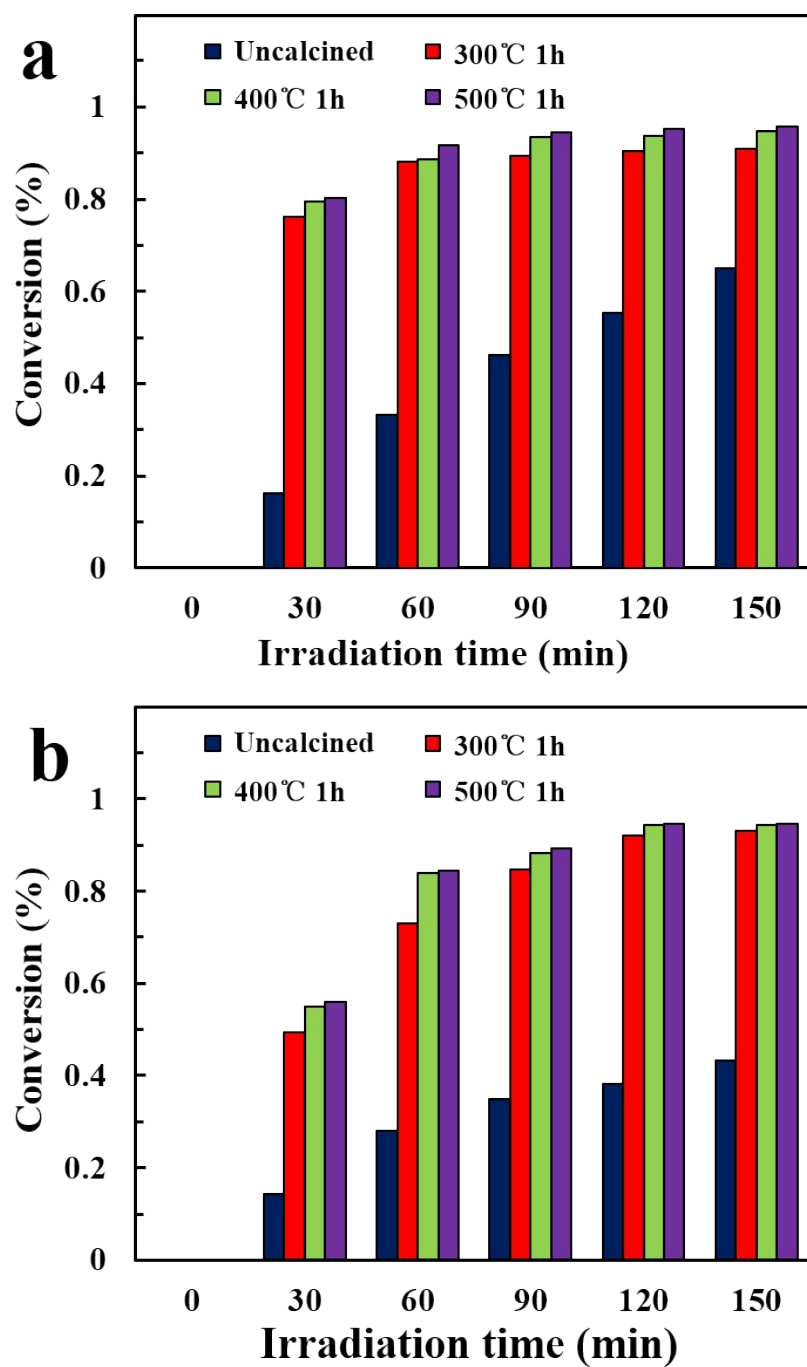


Figure S8. Photocatalytic performances of 9 wt% Au-WO₃ NRs heterostructure calcined at different temperature (i.e., 300, 400, and 500 °C) for 1 h under (a) simulated solar and (b) visible light irradiation ($\lambda \geq 420$ nm).

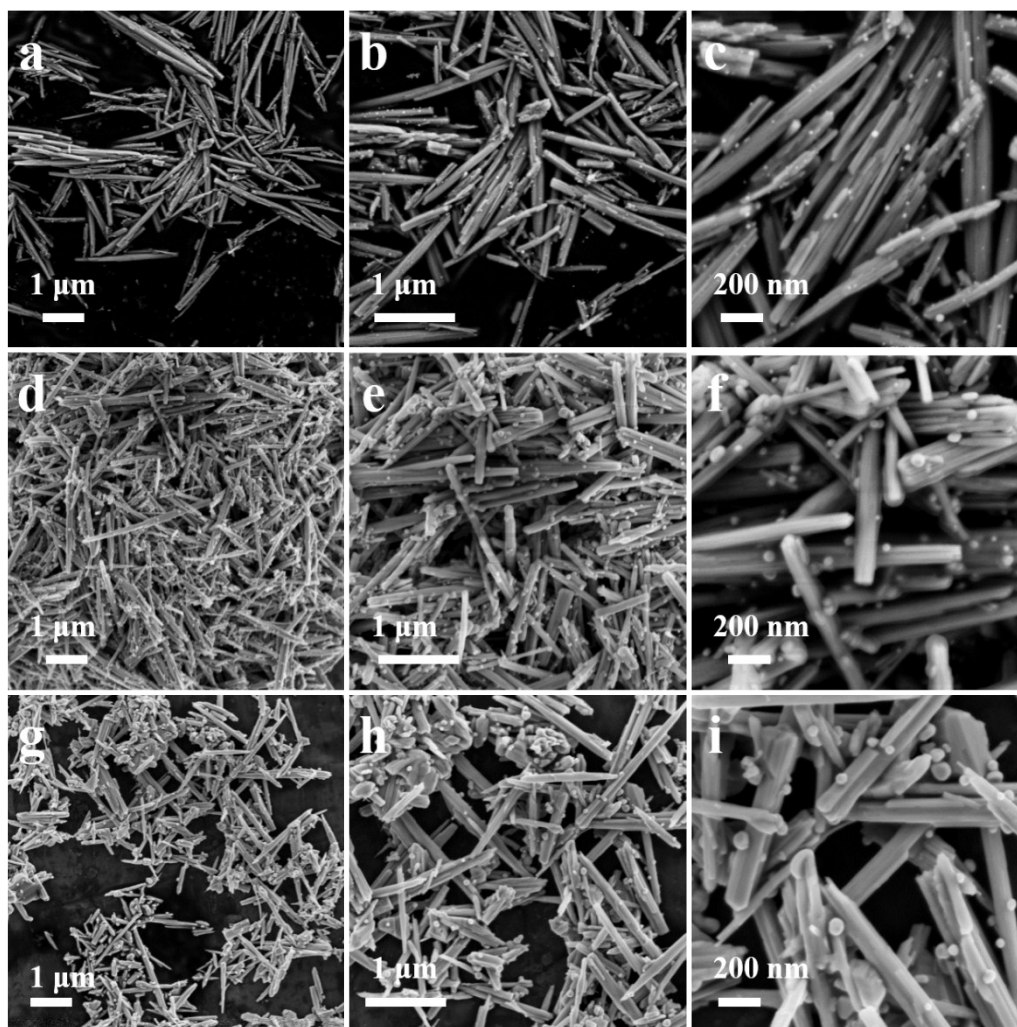
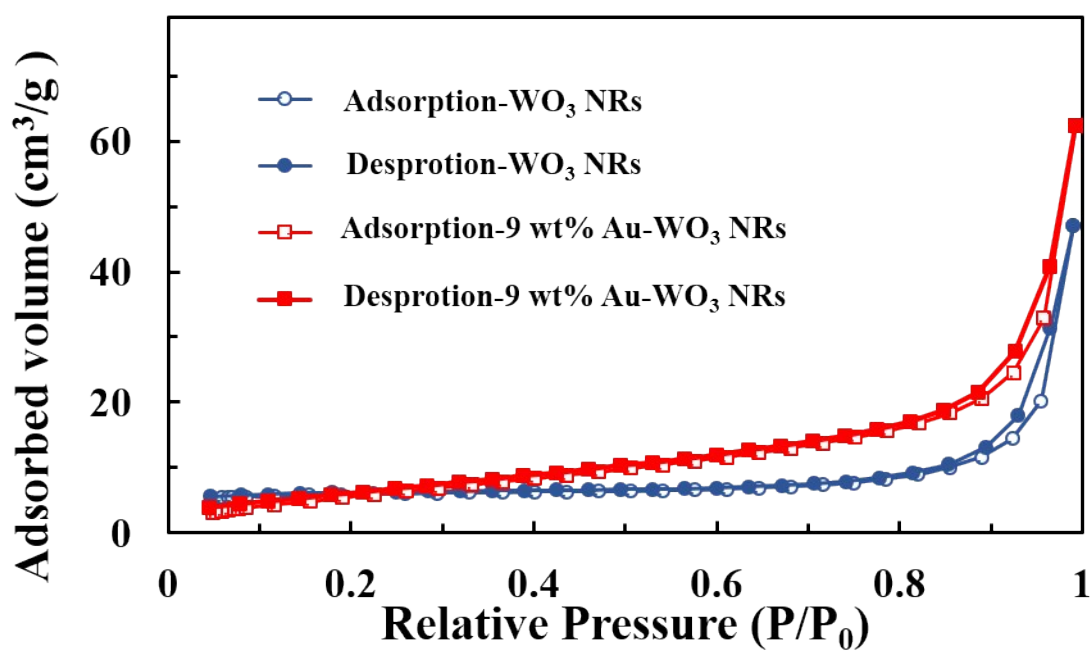


Figure S9. FESEM images of 9 wt% Au-WO₃ NRs heterostructure calcined at (a-c) 300 °C, (d-f) 400 °C and (g-i) 500 °C.



Samples	S_{BET} (m^2/g)	Total pore volume (cm^3/g)	Average pore size (nm)
WO_3 NRs	18.8627	0.06684	16.4216
9 wt% Au- WO_3 NRs	23.1456	0.0966	14.4236

Figure S10. Nitrogen adsorption-desorption isotherms of WO_3 NRs and 9 wt% Au- WO_3 NRs heterostructure. Physicochemical properties of WO_3 NRs and 9 wt% Au- WO_3 NRs heterostructure were summarized in **Table S1**.

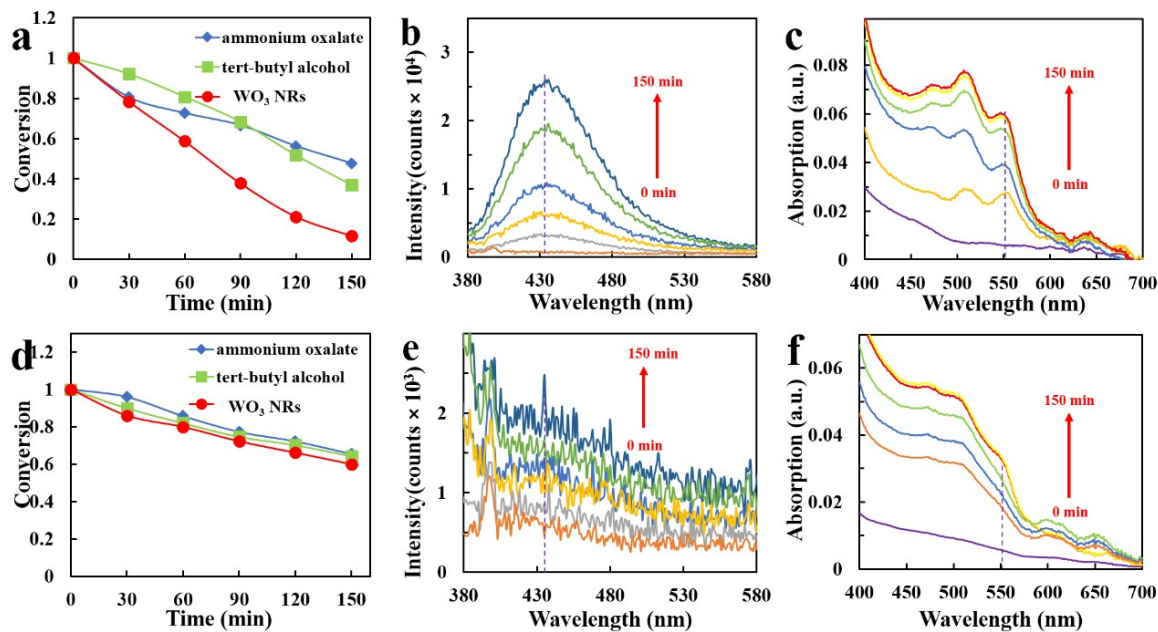


Figure S11. Control experiments with addition of ammonium oxalate (AO) as hole scavenger and tert-butyl alcohol (TBA) as scavenger for hydroxyl radicals under (a) simulated solar and (d) visible light irradiation ($\lambda \geq 420$ nm). PL spectra of WO₃ NRs as a function of irradiation time with an excitation wavelength of 350 nm under (b) simulated solar and (e) visible light irradiation ($\lambda \geq 420$ nm) using TA as a probe molecule. Detection of H₂O₂ signals in WO₃ NRs aqueous dispersion under (c) simulated solar and (f) visible light irradiation ($\lambda \geq 420$ nm).

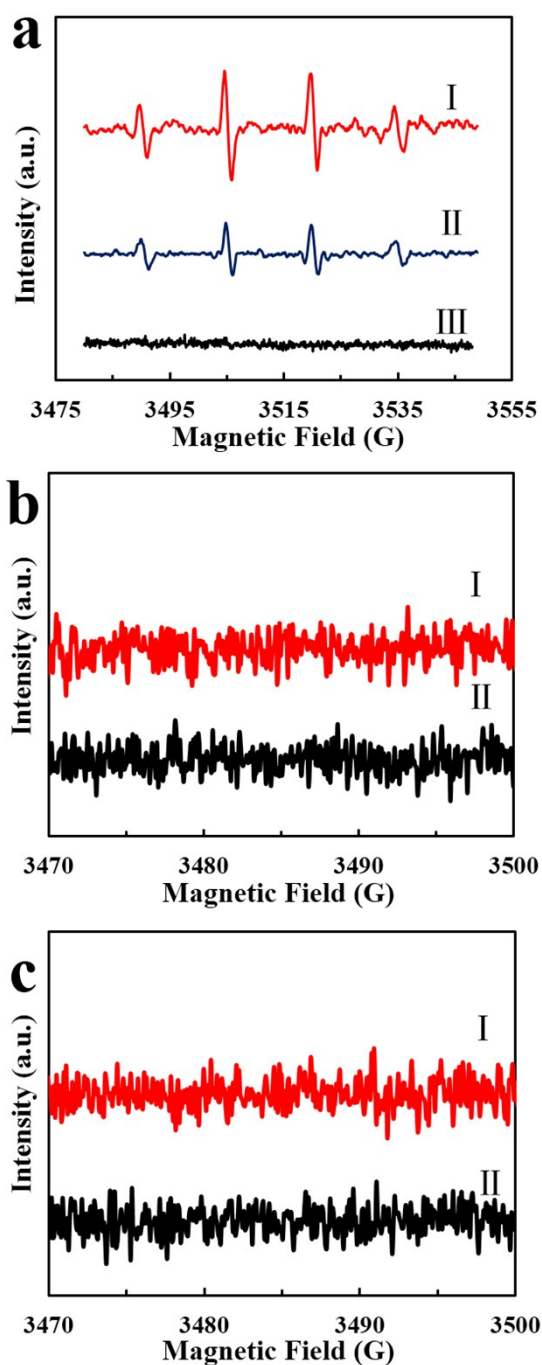


Figure S12. ESR spectra of $\cdot\text{OH}$ radicals (a) trapped by DMPO (DMPO- $\cdot\text{OH}$) for WO_3 NRs (II) and 9 wt% Au- WO_3 NRs composite aqueous suspensions (I) under simulated solar light irradiation and (III) in the dark and $\cdot\text{O}_2^-$ radicals trapped by DMPO (DMPO- $\cdot\text{O}_2^-$) for WO_3 NRs and 9 wt% Au- WO_3 NRs composite aqueous suspension under (b) simulated solar and (c) visible light ($\lambda \geq 420$ nm) irradiation.

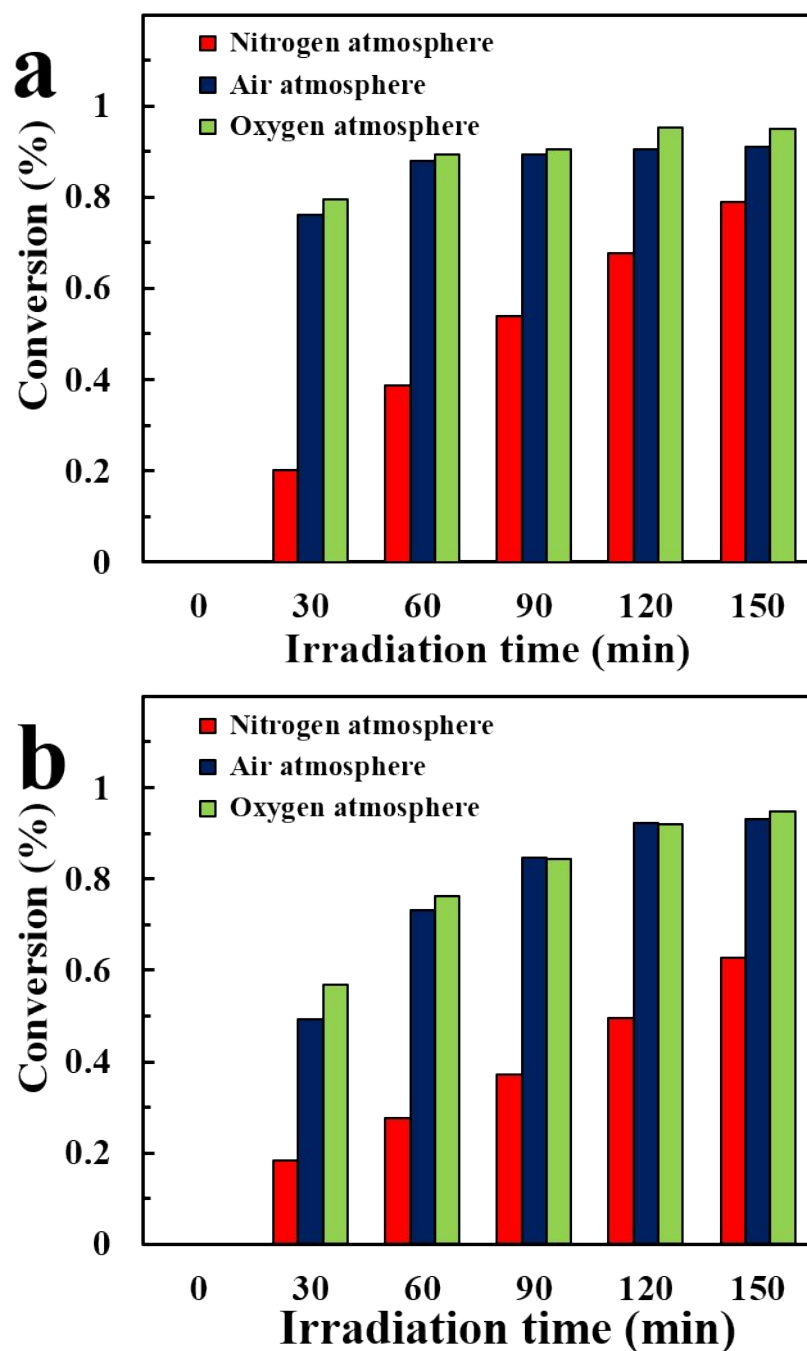


Figure S13. Photocatalytic performances of 9 wt% Au-WO₃ NRs heterostructure in O₂ and N₂ atmospheres under (a) simulated solar and (b) visible light irradiation.

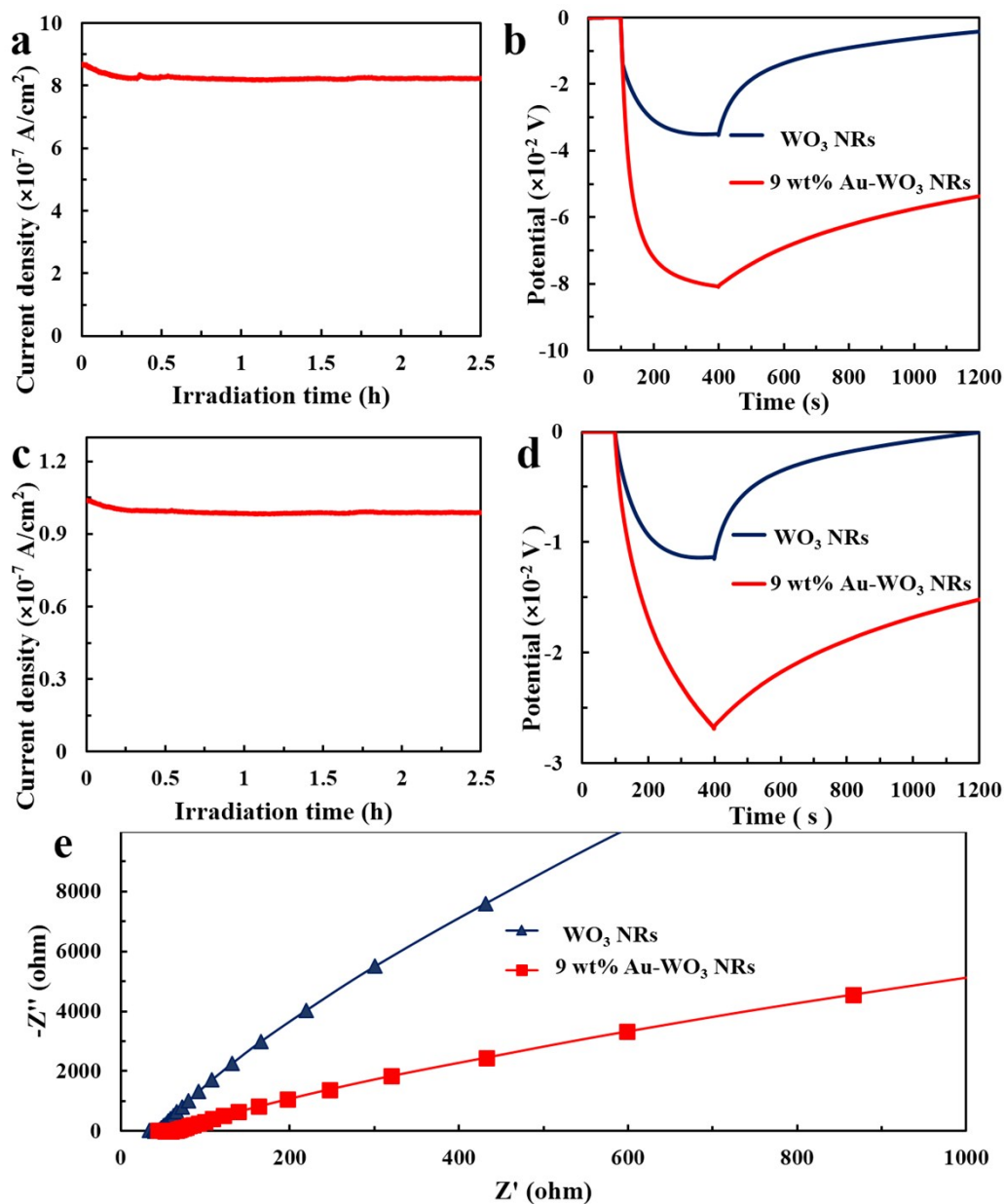


Figure S14. Photocurrents of 9 wt% Au- WO_3 NRs heterostructure under continuous (a) simulated solar and (c) visible light irradiation ($\lambda \geq 420$ nm) for 2.5 h; decay of open circuit potential under (b) simulated solar and (d) visible light irradiation ($\lambda \geq 420$ nm) and (e) EIS results of WO_3 NRs and 9 wt% Au- WO_3 NRs heterostructure in dark.

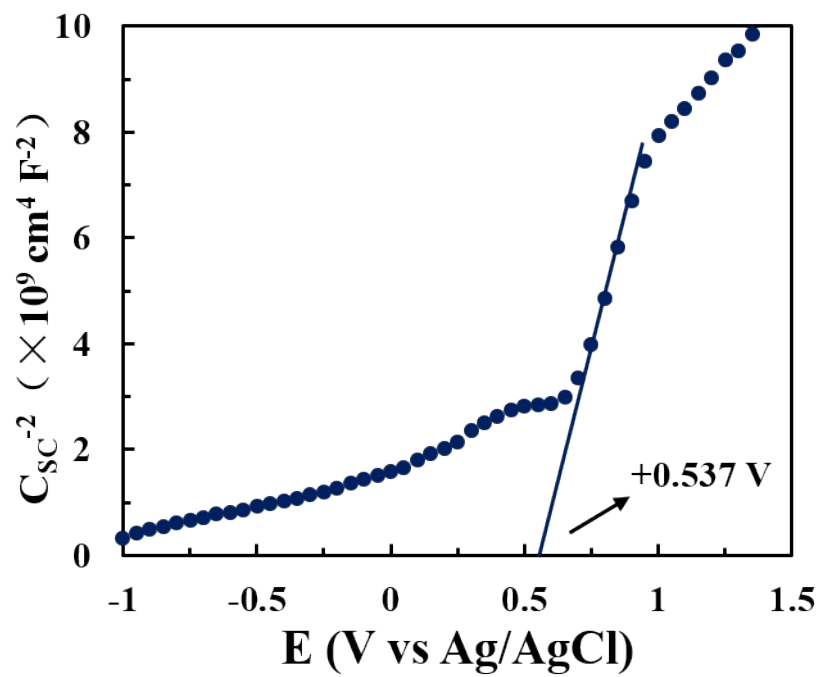


Figure S15. Mott-Schottky plots of WO_3 NRs heterostructure.

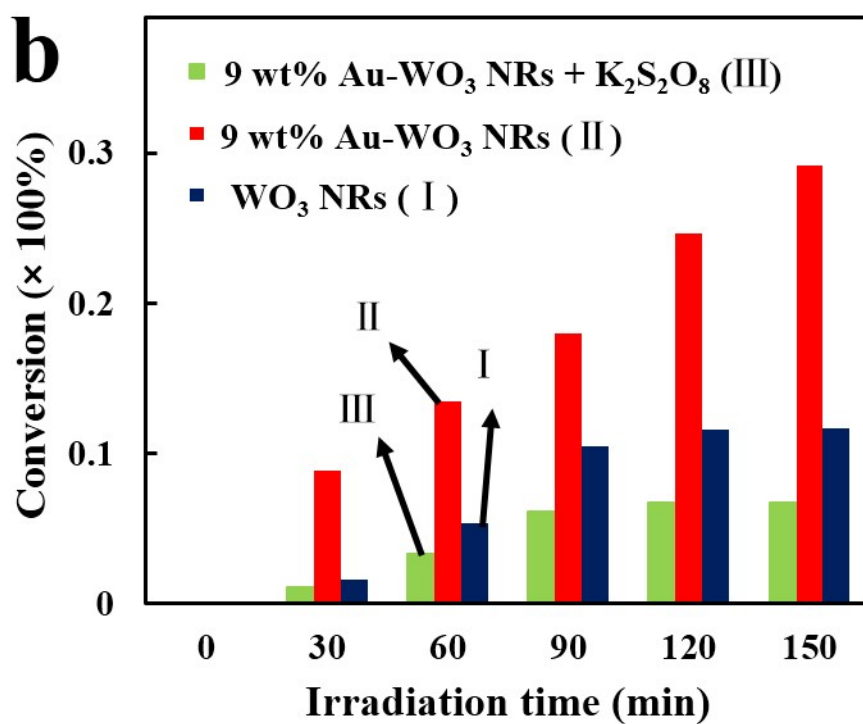
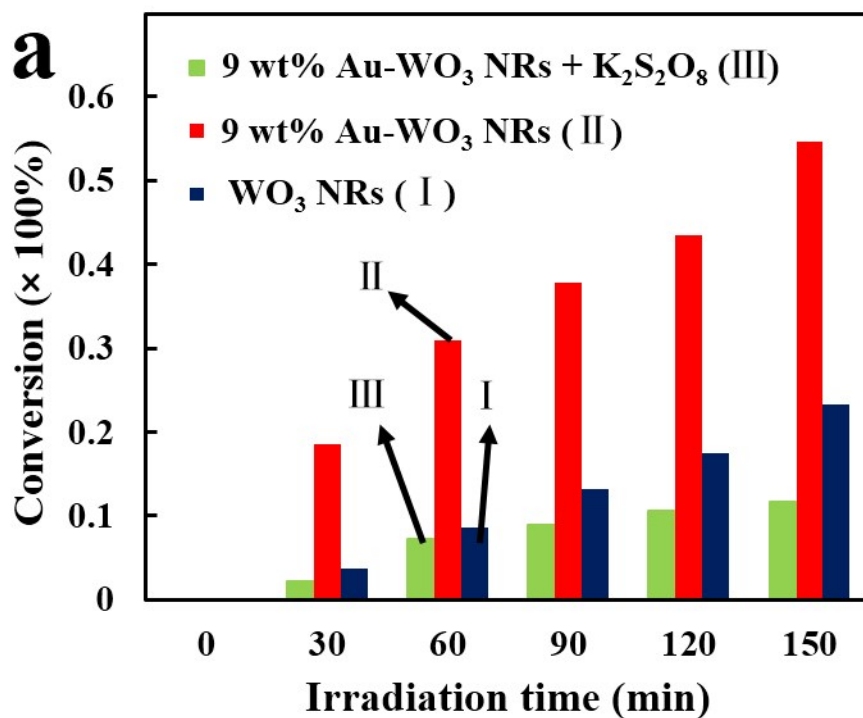


Figure S16. Control experiments with addition of K₂S₂O₈ as electron scavenger under (a) simulated solar and (b) visible light irradiation ($\lambda \geq 420$ nm).

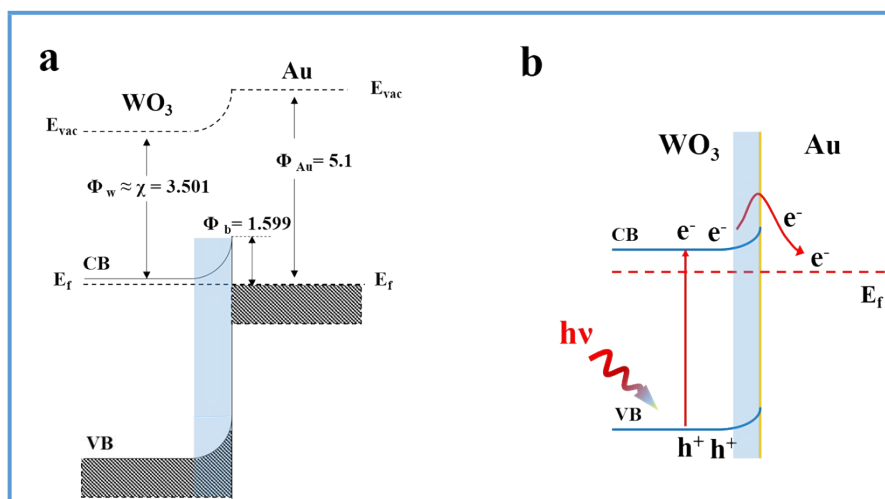


Figure. S17. Schematic illustration depicting the (a) energy-band diagram of Au-WO₃ nanocomposite and (b) schematic band diagram illustrating the charge transfer driven by the Schottky junction. E_{vac} , E_F , Φ_{Au} , Φ_b and χ denote the vacuum level, Fermi level, work function of Au, Schottky barrier height, and electron affinity of WO₃, respectively.

S2. Experimental section

S2.1 Synthesis of negatively charged citrate-stabilized Au NPs (Au@citrate)

The citrate-stabilized gold nanoparticles were prepared by Dotzauer method.^[1] Briefly, all glassware was cleaned thoroughly with aqua regia (3 parts HCl, 1 part HNO₃) and rinsed with deionized water (Milipore, 18.2 MΩ·cm resistivity). In a 1 L Erlenmeyer flask, 50 mL of aqueous 1mM HAuCl₄·3H₂O was heated to a rolling boil with stirring. 5 mL of 38.8 mM sodium citrate dihydrate was also heated to a rolling boil and then added rapidly to the gold solution. After 20s, the mixture became dark and then burgundy, and was subsequently heated with stirring for 10 min and stirred without heating for an additional 15 min.

S2.2 Fabrication of Au@citrate/WO₃ NRs nanocomposite

The prepared Au@citrate aqueous solution (0.18 mg·mL⁻¹) was diluted to a 0.05 mg·mL⁻¹ aqueous solution. The given volume of negatively charged Au@citrate aqueous suspension (0.05 mg·mL⁻¹, pH=10) was added dropwise to the negatively charged WO₃ NRs aqueous dispersion (0.5 mg·mL⁻¹, 200 mL, pH=10) at ambient conditions. The mixture was stirred for 2 h and the precipitation was centrifugated, washed with DI H₂O, and dried in an oven at 60 °C. Finally, the samples were calcinated at 300 °C in air for 1 h giving rise to Au NPs/WO₃ NR nanocomposites.

S3. Calculating method

The conduction band (E_c) and valence bands (E_v) of WO₃ were determined by the following calculation procedures.

1. Calculate electronegativity of the **elements**:²

$$\chi = \frac{I + A}{2}$$

where χ is electronegativity, I is ionization energy and A is electron affinity.

2. Calculate the electronegativity of the **compound M_mO_n**:^{3,4}

$$\chi_{oxide} = [(\chi_M)^m(\chi_O)^n]^{1/(m+n)}$$

3. Calculate the E_g (bandgap) from DRS (UV-visible diffuse reflectance spectra) result:⁵

$$E_g = \frac{1240}{\lambda}$$

4. Determine the E_c and E_v :⁶

vs. Vac (**Vacuum energy level**)

$$E_c = -\chi + 0.5 E_g$$

$$E_v = -\chi - 0.5 E_g$$

vs. SHE (**Standard hydrogen electrode**)

$$E_c = \chi - 4.5 - 0.5 E_g$$

$$E_v = \chi - 4.5 + 0.5 E_g$$

$$E_{CB} = E_{VB} - E_g$$

References

- [1] F. Xiao, *J. Phys. Chem. C* 2012, **116**, 16487.
- [2] R. P. Iczkowski and J. L. Margrave, *J. Am. Chem. Soc.*, 1961, **83**, 3547.
- [3] R. T. Poole, D. R. Williams, J. D. Riley, J. G. Jenkin, J. Liesegang and R. C. G. Leckey, *Chem. Phys. Lett.*, 1975, **36**, 401.
- [4] J. Portier, P. Poizot, G. Campet, M. A. Subramanian and J. M. Tarascon, *Solid State Sci.*, 2003, **5**, 695.
- [5] A. Mylonas, A. Hiskia, E. Androulaki, D. Dimotikali and E. Papaconstantinou, *Phys. Chem. Chem. Phys.* 1999, **1**, 437.
- [6] Y. Xu and M. A. A. Schoonen, *Am. Mineral.* 2000, **85**, 543.